Original Article

Institution of MECHANICAL ENGINEERS
Journal of ENGINEERING IN MEDICINE

Proc IMechE Part H:
J Engineering in Medicine
227(3) 284–292

DOI: 10.1177/0954411912472422
pih.sagepub.com
SAGE

Effect of complex wavelet transform filter on thyroid tumor classification in three-dimensional ultrasound

U Rajendra Acharya[1,2], S Vinitha Sree[3], G Swapna[4], Savita Gupta[5], Filippo Molinari[6], R Garberoglio[7], Agnieszka Witkowska[8] and Jasjit S Suri[3,9]

Abstract

Ultrasonography has great potential in differentiating malignant thyroid nodules from the benign ones. However, visual interpretation is limited by interobserver variability, and further, the speckle distribution poses a challenge during the classification process. This article thus presents an automated system for tumor classification in three-dimensional contrast-enhanced ultrasonography data sets. The system first processes the contrast-enhanced ultrasonography images using complex wavelet transform–based filter to mitigate the effect of speckle noise. The higher order spectra features are then extracted and used as input for training and testing a fuzzy classifier. In the off-line training system, higher order spectra features are extracted from a set of images known as the training images. These higher order spectra features along with the clinically assigned ground truth are used to train the classifier and obtain an estimate of the classifier or training parameters. The ground truth tells the class label of the image (i.e. whether the image belongs to a benign or malignant nodule). During the online testing phase, the estimated classifier parameters are applied on the higher order spectra features that are extracted from the testing images to predict their class labels. The predicted class labels are compared with their corresponding original ground truth to evaluate the performance of the classifier. Without utilizing the complex wavelet transform filter, the fuzzy classifier demonstrated an accuracy of 91.6%, while utilizing the complex wavelet transform filter, the accuracy significantly boosted to 99.1%.

Keywords

Thyroid nodule, contrast-enhanced ultrasound, speckle, complex wavelet transform, benign, malignant, classification, performance

Date received: 13 July 2012; accepted: 29 November 2012

Introduction

More than 50% of the adults have thyroid nodules, of which 7% are likely to be malignant,[1] and the malignancy incidence is increasing at the rate of 3% every year.[2] According to the National Cancer Institute, in the United States, in 2012, the estimated number of new thyroid cases and thyroid-related cancer deaths is 56,460 and 1780, respectively.[3] Therefore, it is important to develop affordable and reliable diagnostic modalities or protocols for better thyroid malignancy management. Medical image analysis can be an effective noninvasive method to detect thyroid malignancies. Among the available thyroid nodule imaging methods, ultrasonography is cost-effective compared to other methods such as computed tomography (CT) and magnetic resonance imaging (MRI).[4] Ultrasonographic imaging does not cause any health hazards unlike CT,

[1]Department of Electronics and Computer Engineering, Ngee Ann Polytechnic, Singapore, Singapore
[2]Department of Biomedical Engineering, Faculty of Engineering, University of Malaya, Kuala Lumpur, Malaysia
[3]Global Biomedical Technologies Inc., Roseville, CA, USA
[4]Department of Applied Electronics and Instrumentation, Government Engineering College, Kozhikode, Kerala, India
[5]Department of Computer Science and Engineering, University Institute of Engineering and Technology (UIET), Punjab University, Chandigarh, Punjab, India
[6]Biolab, Department of Electronics, Politecnico di Torino, Torino, Piedmont, Italy
[7]Scientific Foundation Mauriziana Onlus, Torino, Piedmont, Italy
[8]Department of Internal Medicine, Diabetology and Nephrology, Medical University of Silesia, Zabrze, Silesia, Poland
[9]Department of Biomedical Engineering (Affl.), Idaho State University, Pocatello, ID, USA

Corresponding author:
U Rajendra Acharya, Department of Electronics and Computer Engineering, Ngee Ann Polytechnic, 535 Clementi Road, Singapore 599489, Singapore.
Email: aru@np.edu.sg

which uses harmful radiations. Benign and malignant thyroid nodules have distinguishable sonographic characteristics. Benign nodules have very little internal flow compared to that of malignant nodules.[5] Ultrasound (US) images of the malignant nodule show the presence of a peripheral ring, while it can be present or absent in benign nodule.[5] However, a manual interpretation of these changes is subjective and may result in low diagnostic accuracy. Moreover, speckle noise, which is a granular interference pattern, can also degrade the quality of US images, thus making the diagnostic interpretation difficult. To address these limitations, in this work, we propose a computer-aided diagnostic (CAD) thyroid nodule characterization framework (named after our previous conceptual system—ThyroScan™) that incorporates (1) a complex wavelet transform (CWT) step to reduce the speckle noise, (2) a feature extraction step that uses nonlinear higher order spectra (HOS) information to quantify the sonographic changes that manifest as textural changes in the image, and (3) a classification module that uses the texture features in classifiers to detect the presence or absence of malignancy.

High-resolution ultrasonography (HRUS) is a widely used method for diagnosing thyroid abnormalities,[6] which has resolution high enough to reveal formations with size in the order of 1 mm. In our earlier work, we achieved 100% classification accuracy to detect thyroid malignancy using three-dimensional (3D) HRUS images.[7] HRUS was chosen instead of contrast-enhanced ultrasonography (CEUS) due to the fact that overlapping findings in the case of CEUS limited its potential in distinguishing malignant and benign thyroid lesions. In this article, however, we overcome the limitation of CEUS images by processing it with an intermediate CWT stage. Moreover, the US contrast agent is not potentially nephrotoxic and so CEUS may be a first choice method for thyroid nodule diagnosis especially in patients of high risk of kidney failure.[8] In addition, the contrast agent enhances the vasculature representation of the thyroid in CEUS images, which is useful for distinguishing benign and thyroid nodules. Therefore, we were motivated to develop a reliable CAD system that works on CEUS images.

The objectives of this work are as follows: (1) to show the importance of processing CEUS US images to remove unwanted noise by introducing a CWT stage before features are extracted from the images; (2) to develop an automated system to accurately classify thyroid nodules to benign and malignant; and (3) to use our technique as a reliable adjunct protocol and thereby alleviate the need for the labor-intensive and invasive fine-needle aspiration (FNA) biopsy, which is currently the gold standard,[9] in the early stages of disease management.

Our CAD system is represented in Figure 1. In the off-line training system, after the CWT stage, significant HOS features and ground truth of whether the image is benign or malignant are used to train a fuzzy classifier. In the online system, the trained classifier is used to perform real-time classification of thyroid nodules into benign and malignant. We have thus combined CAD techniques with US image analysis[10] for objective analysis. We compared the performance of the classifier with and without the CWT stage. If CWT stage is not included, HOS features are directly extracted from the raw (i.e. unprocessed (UNPR)) CEUS images. We found that the inclusion of CWT stage resulted in tremendous improvement in the performance of the classifier in distinguishing malignant and benign thyroid nodules.

Patient selection

Thirty patients with the presence of goiter nodule (multinodule goiter cases excluded) were selected for the initial screening tests. A signed informed consent was obtained prior to image acquisition from patients, and approval was also obtained from the ethical committee of the Endocrinology Section of the "Umberto I" Hospital of Torino in Italy. Accurate diagnosis of nodules was done using FNA biopsy and CEUS image examinations. We confirmed that the malignant images obtained had characteristics of malignancy such as intranodular microcalcifications, hypoechoic appearance, and irregular margins.[11] The FNA examination produced the following diagnosis results for the 30 patients: 5 patients had benign goiter nodules that can be classified as THY2 (Group 1: nonneoplastic) and 25 patients had the characteristics of follicular neoplasm. They were classified under the group THY3 (Group 2: follicular lesion/suspected follicular neoplasm) and were subjected to thyroidectomy. Among these 25 patients, 5 had nodule diameter exceeding 6 cm. Manual scanning is inadequate to capture such big lesions, and hence, these patients were excluded from the study. Three patients were excluded since they swallowed and coughed in between the CEUS test, producing motion artifacts in the recorded images. Two cases of concomitant thyroiditis were also eliminated. The short-listed 15 Group 2 patients can be further grouped as follows: 5 benign (follicular neoplasm) cases and 10 malignant cases (7 papillary, 1 follicular neoplasm, and 2 Hurthle cells carcinoma). Thus, including the above-mentioned 10 benign goiter nodule patients (Group 1), we had 10 benign patients and 10 malignant patients. Clinical examination and hormonal profiling were conducted for all the 20 patients. Among these 20 patients, 10 were males (age: 53.5 ± 13.3 years; range: 22–71 years) and 10 females (age: 50.1 ± 10.8 years; range: 25–68 years). The average size of benign/malignant nodules was 31.7 ± 17.9 mm with range of 10–52 mm.

CEUS image acquisition and preprocessing

For acquiring the CEUS images, 2.5 mL of Sonovue (an US contrast agent) was intravenously injected. It

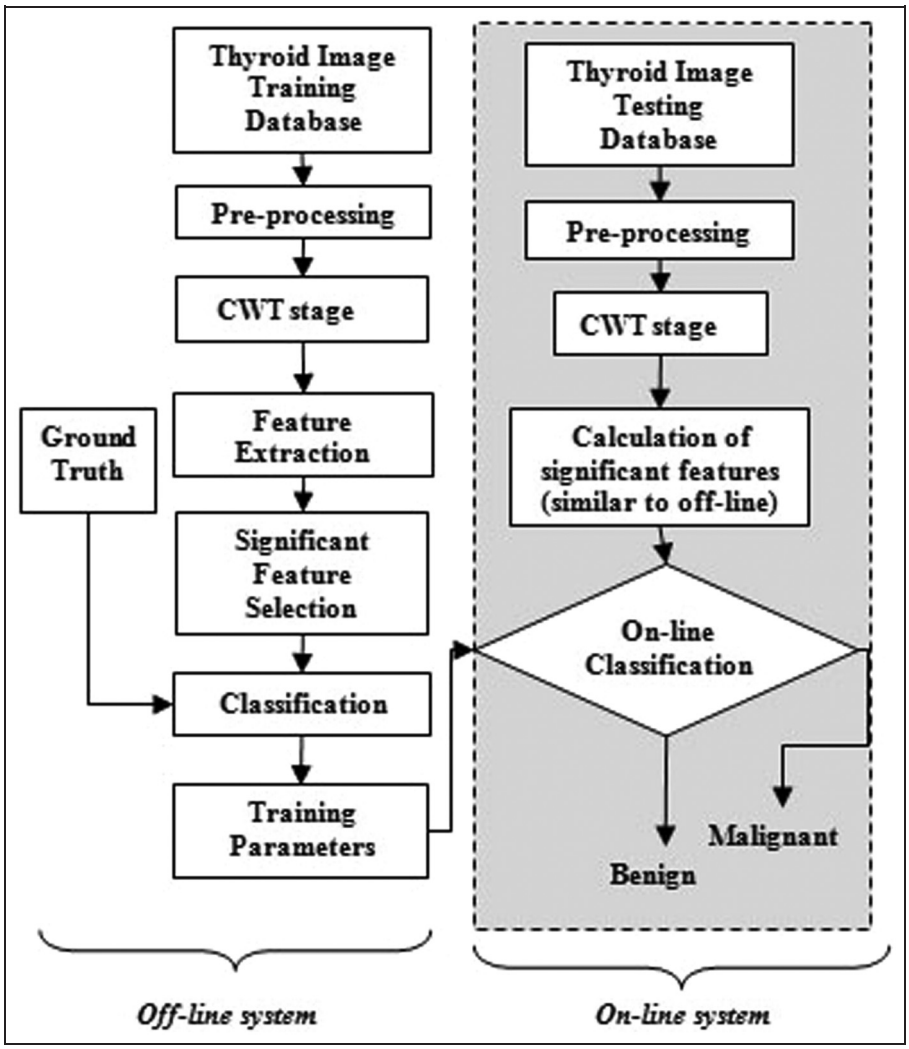

Figure 1. Block diagram of the proposed CAD technique for thyroid nodule characterization; the blocks outside the dotted shaded rectangular box represent the flow in the off-line training system, and the blocks within the dotted box indicate the online system. CWT: complex wavelet transform.

was so arranged that 50 s after the contrast agent was injected, a freehand scanning was performed for all the 20 patients by a trained expert who had more than 30 years of experience in neck ultrasonography. MyLab70 ultrasound scanner (Biosound-Esaote, Genova, Italy) equipped with an LA-522 linear probe that works in the range 4–10 MHz was used. In our work, images were acquired at 5 MHz with an average frame acquisition rate of 16 frames/s. The background average intensity was calibrated to be less than 5 in a 0–255 linear scale. The acquired 3D volumes were transferred to an external workstation in digital imaging and communications in medicine (DICOM) format for further processing and reconstruction. The following are the different stages employed for the processing of the acquired CEUS images:

- Preprocessing stage: All the 3D volume images were initially converted to double precision format. Subsequently, attenuation of the intensity artifacts present in the images was done by applying a linear ramp with decreasing intensity from 1 to 0. This was followed by a normalization stage, a low-pass filtering stage and then an initial speckle noise reduction (using a first-order statistic filter) stage.
- Microbubble detection: All the slices of the 3D CEUS volumes were processed (PR) by morphological opening with a disk-shaped structuring element in order to enhance the microbubble signal. The image points perfused by the contrast agent were then segmented by using the global thresholding method, with the threshold level automatically set by the Otsu's criterion.
- 3D reconstruction: After thresholding, the segmented masks of each slice were grouped together in order to generate the 3D reconstruction of the contrast agent diffusion in space and inside the thyroid nodule. For visualization purposes, the 3D rendered images were also thinned in order to improve the visual perception of the intranodular vascularization.

Full details about the preprocessing, microbubble detection, and 3D reconstruction methods are reported in our previous article.[12]

Forty images were selected from each of the 10 patients with benign nodules and 10 patients with malignant nodules. Thus, 400 benign images and 400 malignant images were used to test the efficiency of the proposed system. Henceforth, we refer to these raw CEUS images of benign and malignant nodules as UNPR images.

Image denoising and grayscale feature extraction

The relevant characteristics of the CEUS images are captured by features. The mapping from images to features is a way of extracting objective information instead of using subjective information. We used CWT for speckle noise reduction and HOS-based analysis methods to extract features.

Image denoising: use of CWT domain filter

Several adaptive filters such as Lee filter, Kaun filter, Frost filter, sigma filter, and gamma maximum a posteriori (MAP) filter have been used to reduce the speckle noise in US images.[13] But it has been observed that these filters lead to suppression of image features and useful information along with speckle noise, causing ambiguity in interpretation. Recently, CWT has established an impressive reputation as a tool for image denoising as it gives much better directional selectivity while maintaining the low redundancy.[14,15] The UNPR CEUS images (Figure 2(a) and (b)) are passed through CWT filter for speckle noise reduction. The PR images are obtained from the output of the CWT filter (Figure 3(a) and (b)).

In this work, the employed CWT filter uses the generalized Nakagami density (GND) function to approximate the speckle statistics under different scattering conditions commonly encountered in medical US images.[16,17] Subsequently, a Bayesian threshold is derived to threshold the high-pass wavelet coefficients of the noisy image. This filter is scale and spatially adaptive as it adapts itself to the local image statistics and speckle statistics that vary from finer to coarser scales.[18] The CWT stage consists of mainly three steps. First, the image is decomposed into several scales through a multiorientation analysis using two-dimensional (2D) CWT. CWT uses filter banks to decompose signals into low- and high-pass components (represented by wavelet coefficients) called subbands. Low-pass subbands give information about slow-varying signal characteristics, while high-pass subbands are indicative of fast changes in the signal as well as noise. Next, the Bayesian thresholding is applied to process the noisy wavelet coefficients (Y) of detail subbands,[19] and finally, the denoised image (X) is synthesized from the PR (thresholded) wavelet coefficients through the inverse CWT.[20,21] CWT decomposes an image $f(t)$, $t = (t_1, t_2) \in R^2$, using a complex scaling function and six complex wavelet functions as

$$f(t) = \sum_{b\in B}\sum_{j\geq j_0}^{J}\sum_{k=-\infty}^{\infty} \mathrm{D}_f(j,k)\psi_{j,k}(t) + \sum_{k=-\infty}^{\infty} \mathrm{C}_f(J,k)\phi_{J,k}(t) \quad (1)$$

where $\phi_{J,k}(t)$ and $\psi_{j,k}(t)$ are complex; $\phi_{J,k} = \phi^{\mathrm{r}}_{J,k} + \sqrt{-1}\phi^{\mathrm{i}}_{J,k}$ and $\psi_{j,k} = \psi^{\mathrm{r}}_{j,k} + \sqrt{-1}\psi^{\mathrm{i}}_{j,k}$. The $\psi^{\mathrm{r}}_{j,k}$ and $\psi^{\mathrm{i}}_{j,k}$ are themselves real wavelets, where $\mathrm{D}_f(j,k)$ and $\mathrm{C}_f(J,k)$ are the wavelet and scaling function coefficients, respectively. J_0 is an arbitrary starting scale for coarsest resolution, and J is an arbitrary finite upper limit for highest resolution with $J > J_0$. The real and imaginary parts of the CWT are computed using separate filter bank structures with wavelet h_{0a}, h_{1a} for the real part and h_{0b}, h_{1b} for the imaginary part. The six subbands of the 2D CWT are labeled as $B = \{+15^\circ, +45^\circ, 75^\circ, -15^\circ, -45^\circ, -75^\circ\}$ for the six oriented directions of the wavelet function. In CWT, complex coefficients of CWT are calculated using a dual tree of wavelet filters, each obtaining the real and imaginary magnitude parts.[21] The implementation of a filtering algorithm in CWT domain is very similar to the discrete wavelet transform (DWT) domain. The principle difference is that the thresholding is applied to the magnitudes of the complex coefficients in order to achieve nearly shift invariance as the small signal shifts

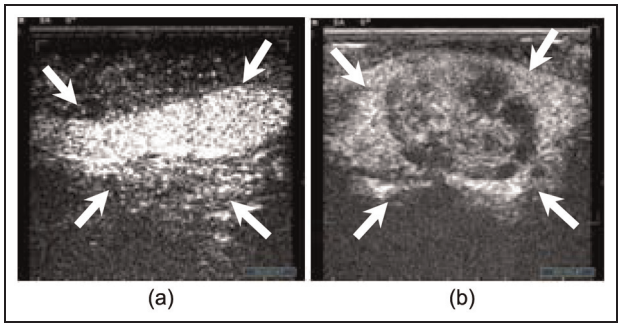

Figure 2. Thyroid CEUS unprocessed images of (a) benign and (b) malignant cases.

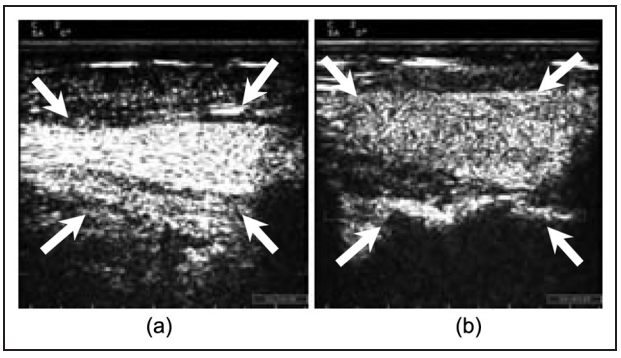

Figure 3. Thyroid CEUS processed images of (a) benign and (b) malignant cases.

may affect the real and imaginary parts keeping the overall magnitude same.

The implementation of the CWT domain-filtering algorithm is summarized as follows:[22]

1. Compute the CWT of the noisy image (f);
2. Specify the value of tuning parameter (K), which controls the degree of noise suppression;
3. Estimate the noise variance (σ^2) using equation (2);
4. For each resolution scale, j, $1 \leqslant j \leqslant J$, and
   For each direction (negative and positive), D, $1 \leqslant D \leqslant 2$;
   For each orientation, $i \in \left\{HH_j^D, LH_j^D, HL_j^D\right\}$;
   For all the spatial locations, $l = 1, 2, \ldots, M$;
   Compute the standard deviation, σ_X, using equations (3), (4) and (6);
   If $\sigma_X > 0$, estimate the coefficient, $\hat{x}_l$, using equation (5), otherwise set $\hat{x}_l = 0$.
5. Apply the inverse CWT to get the denoised image (g)

$$\hat{\sigma}^2 = \left[K\frac{median(|Y_l|)}{0.6745}\right]^2, \quad Y_l \in \{HH_1, HH_2\} \tag{2}$$

$$\sigma_y^2 = \sigma_x^2 + \Omega \tag{3}$$

$$\hat{\sigma}_x^2 = \max\left(\hat{\sigma}_y^2 - \Omega, 0\right) \tag{4}$$

$$\hat{x} = sign(y)\left(\max\left(0, \frac{2s|y|}{B} - \frac{\Omega + \sqrt{\Omega^2 - 8As(s-1)(Ay^2 - \sqrt{2}\Omega y) + 2ABC}}{\sqrt{2}AB}\right)\right) \tag{5}$$

$$\Omega = \left(K_1\sigma^2\right)^s \quad \text{and} \quad K_1 = \frac{m^{1/s}\cdot\Gamma(m)}{\Gamma(m + 1/s)} \tag{6}$$

where $A = ms\sigma_x y^{2s-2}$, $B = 2s(2s-1)$, $C = (2ms-1)\Omega\sigma_x$, and m and s are the shape adjustment parameters of generalized Nakagami distribution. The shrinkage function given in equation (5) named as *GNDThresh* can be easily deployed to derive the thresholding estimators for the density functions belonging to the generalized Nakagami family.[22]

Grayscale feature extraction: HOS

Before the HOS parameters are evaluated, the preprocessed and complex wavelet transformed US images were subjected to Radon transform.[23] The Radon transform rotates the image around its center through different angles θ and then computes line integrals along many parallel paths in the image, transforming the intensity along these lines into points of the resultant signal. Thus, the input for the Radon transform is an image and the output is a one-dimensional signal at various angles. From the one-dimensional signal, HOS parameters are extracted at a constant angle interval of 45° (at 0°, 45°, 90°, 135°, 180°). HOS (polyspectra) is the spectral representation of higher order statistics, that is, moments and cumulants of third and higher order, which can be used for deterministic signals and random processes. Since the HOS of Gaussian signals are statistically zero, it can measure non-Gaussianity and offers good noise immunity. HOS can preserve the true phase information of signals and can detect nonlinearity. HOS features used in this study are derived from the bispectrum. Bispectrum $B(f_1,f_2)$ is the third-order statistics of the signal given by

$$B(f_1,f_2) = E[X(f_1)X(f_2)X(f_1 + f_2)] \tag{7}$$

where $X(f)$ is the Fourier transform of the signal $x(nT)$, n is an integer index, T is the sampling interval, and $E(\cdot)$ is the expectation operator. The frequency f may be normalized by the Nyquist frequency (half of the sampling frequency) for values to lie between 0 and 1. The region Ω of computation of bispectrum and bispectral features of a real signal is uniquely given by a triangle $0 \leqslant f_2 \leqslant f_1 \leqslant f_1 + f_2 \leqslant 1$ as given in Figure 4.

We determined the mean of magnitude as follows

$$mAmp = \frac{1}{L}\sum_{\Omega}|B(f_1,f_2)| \tag{8}$$

The following H parameters, which are related to the moments of bispectrum, were also calculated in this work. The sum of logarithmic amplitudes of bispectrum H_1 is given by

$$H_1 = \sum_{\Omega}\log(|B(f_1,f_2)|) \tag{9}$$

The sum of logarithmic amplitudes of diagonal elements in the bispectrum H_2 is given by

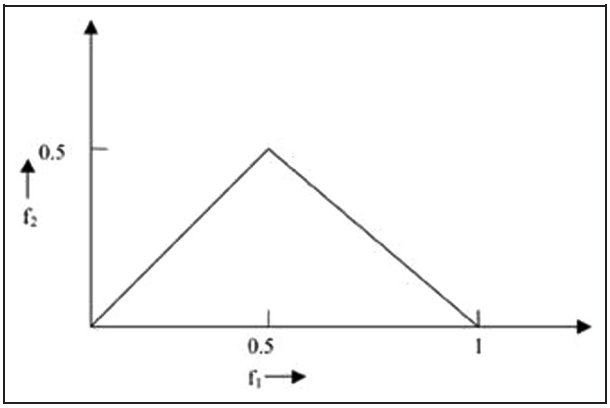

Figure 4. Principal domain or nonredundant region Ω of computation of the bispectrum for real signals. Frequencies are shown normalized by the Nyquist frequency.

$$H_2 = \sum_{\Omega} \log(|B(f_1, f_2)|) \quad (10)$$

The first-order spectral moment of amplitudes of diagonal elements of the bispectrum H_3 is

$$H_3 = \sum_{k=1}^{N} k \log(|B(f_k, f_k)|) \quad (11)$$

$$H_4 = \sum_{k=1}^{N} (k - H_3)^2 \log(|B(f_k, f_k)|) \quad (12)$$

All the above features are defined over a principal domain Ω. L is the number of points within the region Ω. More details of equations for the HOS features *mAmp*, H_1, H_2, H_3, and H_4 are given in the study by Chua et al.[24]

Feature selection

We used Student's *t*-test to study whether the mean value of a feature is significantly different between the benign and malignant groups. The result of the *t*-test is the *p*-value, which is compared with a level of significance (α-level). Popular levels of significance are 5% (0.05), 1% (0.01), and 0.1% (0.001). If the *p*-value is lower than the α-level, it indicates that the feature is powerful enough to be different for the two classes. In this work, we chose α-level as 0.001 and observed that the features had *p*-values even lower than 0.0001 indicating their strength as valuable discriminators of the two classes.

Classification

We chose the fuzzy classifier for developing the data mining framework as fuzzy classifier is a rule-based classifier that is more comprehensible to the end user. We used a subtractive clustering technique using the Sugeno[25] technique to generate a fuzzy inference system (FIS).[26] FIS contains set of fuzzy rules that are used to perform fuzzy inference calculations to obtain the class label of the test data. We used 10-fold stratified cross-validation data resampling technique to train and test the classifiers. A total of 800 data sets belonging to benign and malignant classes were split into 10 parts randomly, such that each part had the same proportion of images from both classes. During the training phase, 9 parts containing 720 images (320 benign and 320 malignant) with the corresponding class label were used to train the classifier and to obtain the classifier parameters. During the test phase, the trained classifiers were used to predict the class of the remaining part (80 samples) of the data set and to calculate the performance measures. This process was repeated nine more times using different test sets. Then, the average of the performance measures obtained for each of the 10 folds was calculated. The efficiency of the classifier to properly classify the images into their correct classes is given by the performance evaluation parameters, namely, sensitivity, specificity, positive predictive value (PPV), and accuracy. High values for the evaluation parameters indicate high classifier performance.

Results

Significant HOS features

Tables 1 and 2 show the significant HOS features (*p*-value < 0.0001) obtained from the PR images (on which CWT was used for speckle noise reduction) and the UNPR (no CWT stage) CEUS images, respectively, for the 90° Radon transform angle. HOS parameters were obtained at an interval of 45° in the range of 0°–180°. We observed that in both the CEUS PR and UNPR data sets, the values of the significant features (*mAmp*, H_1, H_2, H_3, and H_4) remained the same for all the angular measurements. Thus, the significant HOS parameters obtained are unique irrespective of the angle of measurement. All the five HOS parameters were observed to be low for benign compared to malignant group. Therefore, for training the classifiers, we used only the five significant features obtained using the 90° angle in both PR and UNPR cases. The use of this reduced significant feature set makes the design and training of the classifier simpler and faster.

Classification results

The parameters of accuracy, PPV, sensitivity, and specificity were determined using the CEUS-generated

Table 1. Range (mean ± standard deviation) of the significant features that had a *p*-value less than 0.0001 for CEUS processed images.

Feature (90° angle)	Benign	Malignant
mAmp	2.557E + 15 ± 2.475E + 15	4.651E + 15 ± 2.353E + 15
H_1	5.450E + 04 ± 1.349E + 03	5.570E + 04 ± 984
H_2	891 ± 19.0	912 ± 13.6
H_3	2.809E + 04 ± 657	2.874E + 04 ± 461
H_4	7.023E + 11 ± 4.798E + 10	7.525E + 11 ± 3.507E + 10

Table 2. Range (mean ± standard deviation) of the significant features that had a *p*-value less than 0.0001 for CEUS unprocessed images.

Feature (90° angle)	Benign	Malignant
mAmp	3.38 ± 0.128	3.47 ± 7.160E−02
H_1	5.901E + 04 ± 995	6.020E + 04 ± 846
H_2	967 ± 13.6	990 ± 12.1
H_3	3.068E + 04 ± 461	3.135E + 04 ± 376
H_4	9.095E + 11 ± 4.018E + 10	9.720E + 11 ± 3.501E + 10

Table 3. Performance measures of the classifiers.

	UNPR				PR			
Classifier	A	PPV	Sn	Sp	A	PPV	Sn	Sp
Fuzzy	91.6	91.2	93.8	91.6	99.1	98.6	99.8	98.5

A: accuracy; Sn: sensitivity; Sp: specificity (all values in %); UNPR: unprocessed; PR: processed; PPV: positive predictive value.

thyroid images with and without using CWT stage for speckle noise reduction. The results of the classification are shown in Table 3. All the four performance measures had marked improvement in the case of the PR images compared to the UNPR images. We observed that on using the fuzzy classifier on the PR CEUS images, the accuracy went up to 99.1% from 91.6%, which was obtained using the UNPR images. The other parameters also showed similar increase.

Discussion

Literature review

FNA biopsy has the limitation of the need for an expert physician to conduct the test. When combined with carefully chosen parameter extraction methods and CAD-based techniques, US imaging, which is noninvasive and affordable, has emerged as a comparable contender to FNA to differentiate benign and malignant thyroid nodules. It is sensitive enough to serve as a predictor to thyroid malignancy.[11] In US image processing, useful features are extracted to study the image texture differences and echographic patterns to identify the presence of abnormalities in thyroid nodule. In CEUS, malignancy is indicated by the presence of heterogeneous enhancement, while ring enhancement is prominent in benign nodules.[27] Many works have been conducted for automated benign–malignant thyroid nodule characterization. These studies have used techniques such as molecular profiling,[28] genetic markers,[29] elastography,[30] and fluorescent scanning[31] for thyroid nodule classification. Though the objective of all these works is the same, they differ in input data format, features extracted, methods and classifiers used, and classification efficiency.

In the case of US-based studies, color and power Doppler imaging were already ruled out as they were not suitable for 3D microvessel detection due to undesirable color blooming in high-perfusion cases and poor spatial resolution. In one study,[32] the accuracy of quantitative analysis of tumor vascularity on power Doppler sonograms was analyzed, and using vascular indices, an accuracy of only 84.5% was reached. The most significant characteristic of malignant thyroid nodule is the extensive internal flow. CEUS, with intravenously administered contrast agent, can represent micro- and macrovasculature and the internal flow of thyroid nodules much effectively compared to HRUS. Molinari et al.[12] quantified seven vascular parameters, such as vascular density, number of branching nodes, and so on, for 3D CEUS benign and malignant images but did not use them for classification. Therefore, in 2011, our team worked on developing data mining strategies that use significant features from HRUS and CEUS images for thyroid nodule characterization and classification. In one study,[7] we used 3D HRUS data set to obtain five features, of which three were texture features and two were DWT features, and used them in an AdaBoost classifier with perceptron as weak learner to achieve 100% accuracy, sensitivity, and specificity. In another recent study,[33] we extracted 10 significant features (3 texture features and 7 DWT features) from 3D CEUS thyroid images to obtain an accuracy of 98.9%, sensitivity of 98%, and specificity of 99.8% using k-nearest neighbor (KNN) classifier. Thus, even though HRUS image analysis has reached its perfection in terms of classifier performance,[7] we observed that there is still scope for improvement of detection accuracy using CEUS images.[33] These were the reasons behind choosing CEUS data for this study.

Key features of this study

In this study, we used Sonovue that is a microbubble-based contrast agent that does not come out of the vessel lumen. Any echo received from a microbubble is an indication of the presence of a vessel.[34] Hence, CEUS with Sonovue will give a better depiction of vascularity. We have included CWT to process CEUS images before the extraction of HOS features to deal with speckle noise. Our proposed technique has the following features:

- Ultrasonography, in addition to being affordable and noninvasive, is highly effective and safe. It can detect thyroid nodules as small as 3 mm.[35] US waves are not known to cause any health hazards, they are absolutely safe.
- We used 3D imaging instead of 2D, so that the feature of nodule volume can also be utilized for diagnosis.
- The CEUS data acquisition method is low cost and the proposed automation system consists of algorithms implemented in software that are also affordable.
- The CWT stage suppresses the disturbances in US images such as echo perturbations and speckle noise and preserves features better than DWT. It is especially useful in CEUS images, which contain

strong diagonal features as CWT preserves features oriented at angles 45° and −45° without combining them. Ours is the only work that includes CWT for processing of US images. Due to good shift invariance (as the shrinkage rule is applied to the magnitude of each of the complex coefficients) and good directional sensitivity of CWT, our CEUS image filtering techniques yielded better performance than the earlier DWT-based methods.

- Computational complexity of CWT is low, making it suitable for online real-time applications.
- We have validated our speckle reduction results (obtained after CWT stage) both qualitatively (from two radiologists) and quantitatively in terms of various image quality parameters such as carrier-to-noise ratio (CNR), signal-to-ratio (SNR), and edge preservation index.[21] Detailed results are submitted in an article that is under review. Furthermore, the efficiency of CWT stage is cross-validated by the classifier that results in 99.1% accuracy.
- We avoided the common problem of classifier overfitting by adopting 10-fold cross-validation technique for data resampling.
- The number of significant features to be given as input to the classifier to obtain very high accuracy is very less (just five features) for PR as well as UNPR CEUS images. This makes the design and training of the classifier simpler.
- The fuzzy classifier resulted in the highest accuracy of 99.1% for the PR images, which is higher than previously published results.
- Instead of using the commonly used vascular and texture features, we have, in this work, exploited the capability of popular nonlinear dynamics theory–based HOS features to classify thyroid lesions and achieved the maximum possible accuracy.

Conclusions

Thyroid malignancy analysis using ultrasonography is a noninvasive, affordable, and safe diagnostic test, which produces images depicting the prominent structure and features of thyroid nodule. We have investigated the implication of introducing CWT stage for speckle noise reduction before HOS features are extracted from CEUS images. We have demonstrated that the initial processing of CEUS images with CWT stage significantly improves the efficiency of the automated real-time system in characterizing the thyroid nodules into benign and malignant classes. The fuzzy classifier resulted in the highest accuracy of 99.1% for the CWT PR images, sensitivity of 99.8%, specificity of 98.5%, and PPV of 98.6%.

Funding

This research received no specific grant from any funding agency in the public, commercial, or not-for-profit sectors.

References

1. Lansford CD and Teknos TN. Evaluation of the thyroid nodule. *Cancer Control* 2006; 13: 89–98.
2. ACS (American Cancer Society). What are the key statistics about thyroid cancer? http://www.cancer.org/Cancer/ThyroidCancer/DetailedGuide/thyroid-cancer-key-statistics
3. NCI (National Cancer Institute) on thyroid cancer. http://www.cancer.gov/cancertopics/types/thyroid
4. Soto GD, Halperin I, Squarcia M, et al. Update in thyroid imaging. The expanding world of thyroid imaging and its translation to clinical practice. *Hormones (Athens)* 2010; 9: 287–298.
5. Ivanac G, Brkljacic B, Ivanac K, et al. Vascularization of benign and malignant thyroid nodules: CD US evaluation. *Ultraschall Med* 2007; 28: 502–506.
6. Polyzos SA, Kita M and Avramidis A. Thyroid nodules—stepwise diagnosis and management. *Hormones (Athens)* 2007; 6: 101–119.
7. Acharya UR, Faust O, Sree SV, et al. ThyroScreen system: high resolution ultrasound thyroid image characterization into benign and malignant classes using novel combination of texture and discrete wavelet transform. *Comput Methods Programs Biomed* 2012; 107: 233–241.
8. Claudon M, Cosgrove D, Albrecht T, et al. Guidelines and good clinical practice recommendations for contrast enhanced ultrasound (CEUS)—update 2008. *Ultraschall Med* 2008; 29: 28–44.
9. Baloch ZW, Fleisher S, LiVolsi VA, et al. Diagnosis of follicular neoplasm: a gray zone in thyroid fine-needle aspiration cytology. *Diagn Cytopathol* 2002; 26: 41–44.
10. Suri JS, Kathuria C and Molinari F. *Atherosclerosis disease management*. New York: Springer, 2011.
11. Bastin S, Bolland MJ and Croxson MS. Role of ultrasound in the assessment of nodular thyroid disease. *J Med Imaging Radiat Oncol* 2009; 53: 177–187.
12. Molinari F, Mantovani A, Deandrea M, et al. Characterization of single thyroid nodules by contrast-enhanced 3-D ultrasound. *Ultrasound Med Biol* 2010; 36: 1616–1625.
13. Gupta S, Chauhan RC and Saxena SC. Homomorphic wavelet thresholding technique for denoising medical ultrasound images. *J Med Eng Technol* 2005; 29: 208–214.
14. Kingsbury N. The dual tree complex wavelet transform: a new technique for shift invariance and directional filters. In: *Proceedings of 8th IEEE DSP workshop*, Bryce Canyon, IEEE; Utah, USA; August 1998.
15. Dudy A and Singh K. A new approach for denoising ultrasonographic Images using DTCWT. *Int J Latest Res Sci Technol* 2012; 1: 106–108.
16. Shankar PM. Ultrasonic tissue characterization using a generalized Nakagami model. *IEEE T Ultrason Ferr* 2001; 48: 1716–1720.
17. Gupta S, Chauhan RC and Saxena SC. Robust non-homomorphic approach for speckle reduction in medical ultrasound images. *Med Biol Eng Comput* 2005; 43: 189–195.
18. Pizurica A, Philips W, Lemahieu I, et al. A versatile wavelet domain noise filtration technique for medical imaging. *IEEE T Med Imaging* 2003; 22: 323–331.
19. Jansen M. *Noise reduction by wavelet thresholding* (Lecture notes in Statistics). New York, Springer Verlag, 2001, p. 161.
20. Gupta S, Kaur L, Chauhan RC, et al. A wavelet based statistical approach for speckle reduction in medical

ultrasound images. In: *IEEE proceedings TENCON*, vol. 2, 15–17 October 2003, Bangalore, IEEE, pp. 534–537.
21. Achim A, Bezerianos A and Tsakalides P. Novel Bayesian multiscale method for speckle removal in medical ultrasound images. *IEEE T Med Imaging* 2001; 20: 772–783.
22. Gupta S, Chauhan RC and Saxena SC. A versatile technique for visual enhancement of medical ultrasound images. *Digit Signal Process* 2007; 17: 542–556.
23. Ramm A and Katsevich A. *The Radon transform and local tomography*. Boca Raton, FL, USA, CRC Press, 1996.
24. Chua KC, Chandran V, Acharya UR, et al. Application of higher order statistics/spectra in biomedical signals—a review. *Med Eng Phys* 2010; 32: 679–689.
25. Sugeno M. *Industrial applications of fuzzy control*. New York, NY, USA, Elsevier Science Pub. Co., 1985.
26. Ross TJ. *Fuzzy logic with engineering applications*. West Sussex: John Wiley & Sons Ltd, 2004.
27. Zhang B, Jiang YX, Liu JB, et al. Utility of contrast-enhanced ultrasound for evaluation of thyroid nodules. *Thyroid* 2010; 20: 51–57.
28. Finley DJ, Zhu B, Barden CB, et al. Discrimination of benign and malignant thyroid nodules by molecular profiling. *Ann Surg* 2004; 240: 425–436.
29. Cerutti JM, Delcelo R, Amadei MJ, et al. A preoperative diagnostic test that distinguishes benign from malignant thyroid carcinoma based on gene expression. *J Clin Invest* 2004; 113: 1234–1242.
30. Hong Y, Liu X, Li Z, et al. Real-time ultrasound elastography in the differential diagnosis of benign and malignant thyroid nodules. *J Ultrasound Med* 2009; 28: 861–867.
31. Patton JA, Hollifield JW, Brill AB, et al. Differentiation between malignant and benign solitary thyroid nodules by fluorescent scanning. *J Nucl Med* 1976; 17: 17–21.
32. Lyshchik A, Moses R, Barnes SL, et al. Quantitative analysis of tumor vascularity in benign and malignant solid thyroid nodules. *J Ultrasound Med* 2007; 26: 837–846.
33. Acharya UR, Faust O, Sree SV, et al. Cost-effective and non-invasive automated benign and malignant thyroid lesion classification in 3D contrast-enhanced ultrasound using combination of wavelets and textures: a class of ThyroScan™ algorithms. *Technol Cancer Res Treat* 2011; 10: 371–380.
34. Schneider M, Arditi M, Barrau MB, et al. BRI: a new ultrasonographic contrast agent based on sulfur hexafluoride-filled microbubbles. *Invest Radiol* 1995; 30: 451–457.
35. Mandel SJ. Diagnostic use of ultrasonography in patients with nodular thyroid disease. *Endocr Pract* 2004; 10: 246–252.